EFFECT OF PIEZOELECTRIC ENERGY HARVESTING ON THE RESPONSE OF A GENERATOR WING TO A TURBULENCE GUST

Carlos De Marqui Júnior*, Marcos José Maria*
***Department of Aeronautical Engineering, Engineering School of Sao Carlos**
University of Sao Paulo, Brazil

***Universidade de São Paulo, São Carlos, SP, 13566-590,** BRAZIL

Keywords: *energy harvesting, piezoelectricity, finite element modeling, aeroelasticity*

Abstract

Unmanned Air Vehicles (UAVs) and Micro Air Vehicles (MAVs) are remotely operated aircraft with severe mass, volume and energy sources restrictions. Converting the waste vibration energy available in the environment into electrical energy is the goal of vibration-based energy harvesting. An additional source of energy can be obtained for UAVs or MAVs through the concept of vibration energy harvesting. In this work a piezoelectric generator wing is modeled for energy harvesting from flow excitations. The main motivation is to convert aeroelastic vibrations into electrical energy using the direct piezoelectric effect. The piezoaeroelastic responses of the generator wing to a 1-cos gust disturbance are investigated at several airflow speeds for a set of electrical load resistances in the electrical domain. Continuous and segmented electrodes configurations are investigated and electrical power output and tip displacement for both configurations are presented. The resistive shunt damping effect of piezoelectric power generation is also investigated.

1 Introduction

The major limitation for small UAVs and MAVs is the energy required for long endurance missions [1]. The limited available volume and the energy sources reduce the endurance and the flight range. Generating usable electrical energy during the mission of a UAV can relieve the auxiliary power drains or provide the power required by its sensors. Additional energy sources can be obtained by harvesting solar and vibration energy [2-6].

The concept of energy harvesting has been pointed out as a future breakthrough technology for UAV and MAV design [7]. An additional task to the primary load-bearing function of these aircraft structures is to provide an additional source of electrical energy by converting the vibrations available in their environment to electricity. Researchers have added solar panels [2,3] over the wing skin of UAVs to power small electronic devices or to charge batteries for night flight missions. Another source of energy for UAVs is the mechanical vibration energy due to unsteady aerodynamic loads during the flight [2] or due to ground excitation in perching [3,6]. Piezoelectric transduction has received the most attention for vibration-based energy harvesting due to the large power densities and ease of applications [7-10]. The concept of self-charging structures [11] has been introduced to improve multifunctionality in UAVs. The proposed multilayer structure is composed of piezoceramic layers for vibration-to-electric energy conversion, thin-film battery layers for storing the generated energy and a metallic substructure layer as the original load-bearing layer.

The literature of aeroelasticity includes research on using active controllers with piezoelectric elements and other types of smart materials as actuators to modify the aeroelastic behavior of

wings [12]. The effect of passive controllers on the aeroelastic response of a structure has also been investigated by some authors [13-15]. The main goal in these papers is to increase overall damping of the aeroelastic system by employing piezoelectric materials with an external shunt circuit.

Some authors have investigated the conversion of aeroelastic vibrations to electricity. Bryant and Garcia [16] presented the modeling of a two-degree-of-freedom typical section as a piezoelectric power harvesting device driven by aeroelastic vibrations. The main motivation is to have an alternative energy source for placement in urban areas. A switching energy extracting scheme is used in order to increase the power extraction of the aeroelastic energy harvester.

Recently, time-domain piezoaeroelastic modeling of a piezoelectric generator wing with embedded piezoceramics has been presented in the literature [4,17]. The model is obtained from the combination of an electromechanically coupled finite element (FE) model [18] with an unsteady aerodynamic panel model. Although the flutter instability is usually avoided in a real aircraft, it is the simplest case for the concept demonstration of a generator wing using the linear piezoaeroelastic model. The response history with the largest instantaneous power output at the flutter speed shows a decaying behavior that is due to the shunt damping effect of power generation. The effect of using segmented electrodes on the piezoaeroelastic response of the same generator wing and the same set of load resistances has also been investigated [4]. The electrodes are segmented on the center line (mid-chord position) and properly combined to the electrical load to avoid the cancelation of the potential electrical output of the torsion-dominated modes (which is strongly cancelled when continuous electrodes are used). As a consequence of the improved electromechanical coupling, better power generation and shunt damping effects are obtained for the aeroelastic behavior since the piezoelectric reaction of the torsional modes in the coupled aeroelastic motions of flutter are taken into account with the segmented-electrode configuration.

Although the time-domain linear piezoaeroelastic model can be used to simulate the piezoaeroelastic response at different airflow speeds, the vortex lattice model is computationally expensive for repeated simulations. This way such a model is not practical to determine the optimum elements in the energy harvesting circuit of the generator wing. Therefore, a frequency domain piezoaeroelastic model for energy harvesting was presented [5]. The doublet-lattice model is associated with the electromechanically coupled finite element model. A modified p-k solution is used to solve the piezoaeroelastic equations. Piezoaeroelastically coupled frequency response functions are also presented for several airflow speeds.

In this work the piezoaeroelastic time domain solution is presented for energy harvesting. In the previous works, a sharp edge gust was used as the main excitation to the generator wing. Here, the response of the piezoaeroelastic wing to a 1-cos gust disturbance is investigated.

2 A piezoaeroelastic finite element model

The piezoaeroelastic model is obtained by combining an electromechanically coupled FE model [9] and an unsteady Vortex Lattice Method (VLM) [17,18]. The electromechanically coupled FE model is based on the Kirchhoff assumptions to model the thin cantilevered wing with embedded piezoceramic layers shown in Figure 1. The piezoceramic layers (which are poled in the thickness direction) are covered by continuous electrodes (which are assumed to be perfectly conductive) of negligible thickness. A rectangular finite element with four nodes and three mechanical degrees of freedom per node is used to model the substructure. An electrical degree of freedom is added to the finite element to model the piezoceramic layers (13 degrees of freedom in total).

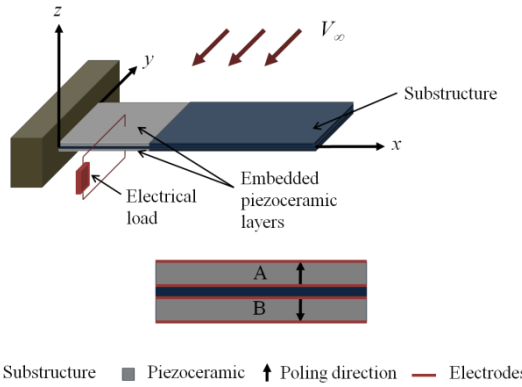

Fig. 1. A piezoelectric power generator wing under flow excitation and the cross-sectional view of the region with embedded piezoceramics and continuous electrodes.

The governing piezoaeroelastic equations for the generator wing are

$$\mathbf{M}\ddot{\boldsymbol{\Psi}} + \mathbf{C}\dot{\boldsymbol{\Psi}} + \mathbf{K}\boldsymbol{\Psi} - \tilde{\boldsymbol{\Theta}} v_p = \mathbf{F} \qquad (1)$$

$$C_p \dot{v}_p + \frac{v_p}{R_l} + \tilde{\boldsymbol{\Theta}}^t \dot{\boldsymbol{\Psi}} = 0 \qquad (2)$$

where $\mathbf{M}$ is the global mass matrix, $\mathbf{K}$ is the global stiffness matrix, $\mathbf{C}$ is the global damping matrix (assumed here as proportional to the mass and stiffness matrices), $\tilde{\boldsymbol{\Theta}}$ is the effective electromechanical coupling vector, $\boldsymbol{\Psi}$ is the vector of mechanical coordinates (nodal mechanical variables), C_p is the effective capacitance of the piezoceramic, R_l is the load resistance and v_p is the voltage across the load [9]. The right-hand-side term $\mathbf{F}$ in Equation (1) represents the unsteady aerodynamic loads obtained using the unsteady VLM.

The bimorph cross-section shown in Figure 1 allows combining the electrical outputs of the upper (A) and the lower (B) piezoceramic layers either in series or in parallel.

For a torsional vibration mode with the nodal line corresponding to the center line of the width, strong cancellations occur in both layers (A and B) of the configuration shown in Figure 1.

2.1 Unsteady Aerodynamic Model

An unsteady VLM is used to obtain the loads over a cantilever plate-like wing [17,18]. The wing is represented as a thin lifting surface and it is divided into a number of elements (panels). A planar vortex ring is associated with each rectangular panel of the body itself and its wake. The vortex singularity is a solution for the Laplace equation and the aerodynamic loads on the wing can be obtained by combining these singularities with the incompressible potential flow around the body.

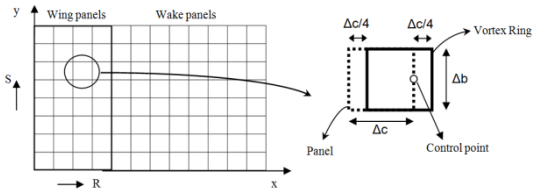

Fig. 2. Vortex-lattice mesh for a cantilevered wing.

A typical vortex-lattice mesh for the three-dimensional flow problem is shown in Figure 2. The leading segment of each vortex ring is placed at the quarter chord point of each panel and a control point is placed at the three-quarter chord of each panel, where the boundary condition is verified. If the surface of the plate-like wing has m panels ($m = R \times S$, where R and S are the number of panels along the chord and the span, respectively) and consequently m vortex rings and control points, one can express the boundary condition as:

$$\mathbf{a}_{KL}\boldsymbol{\Gamma}_{m,1} = \left[\mathbf{v}_{m_{m,1}} + \mathbf{v}_{w_{m,1}}\right] \cdot \mathbf{n}_{m,1} \qquad (3)$$

where $\mathbf{a}_{KL}$ is the influence coefficient that relates the circulation at the vortex ring K to the inner product of the perturbed velocity at point L. Both counters K and L can have values from 1 to $R \times S$. For example to scan all the vortex rings influencing the control point K, an inner scanning loop is need with the counter $L = 1 \rightarrow S \times R$. The unknowns in this linear set of equations are the circulations Γ_m of each vortex ring. The term $\mathbf{v}_m$ is always known at each time step as it depends on the free stream velocity and the velocities of the control points due to structural deformations. The velocities induced by the wake $\mathbf{v}_w$ are also known at each time step. New vortex rings are formed and shed

from the trailing edge to the wake at each time step and the Kutta condition is satisfied imposing the circulation values of the most recently shed vortex rings are the same as those at the trailing edge (shedding vortices) in the previous time step. The circulation values for the vortex rings placed on the wing are obtained from the solution of the linear system given by Equation (3). The aerodynamic load for each panel can then be calculated from the unsteady Bernoulli equation [17,18].

2.2 Combination of the Models and the Numerical Integration Scheme

The equations of motion obtained from the FE formulation can be represented in modal domain as:

$$\bar{\mathbf{M}}\ddot{\boldsymbol{\eta}}+\bar{\mathbf{C}}\dot{\boldsymbol{\eta}}+\bar{\mathbf{K}}\boldsymbol{\eta}-\boldsymbol{\Phi}^t\tilde{\boldsymbol{\Theta}}v_p=\boldsymbol{\Phi}^t\mathbf{F} \tag{4}$$

$$C_p\dot{v}_p+\frac{v_p}{R_l}+\tilde{\boldsymbol{\Theta}}^t\boldsymbol{\Phi}^t\dot{\boldsymbol{\eta}}=0 \tag{5}$$

where $\boldsymbol{\eta}$ is the vector of modal coordinates, $\boldsymbol{\Phi}$ is the modal matrix (mass normalized so that the modal mass $\bar{\mathbf{M}}$ is the identity matrix), $\bar{\mathbf{C}}$ is the diagonal modal damping matrix, $\bar{\mathbf{K}}$ is the diagonal modal stiffness matrix and $\mathbf{F}$ is the vector of aerodynamic loads. This is the decoupled form [9] of the equations of motion (in the modal sense), hence the solution can be performed considering the most significant modes in the aeroelastic problem.

The solution of this piezoaeroelastic model in time domain has a particular complication: the dependence between the electromechanical solution and the aerodynamic solution which are originally solved for distinct meshes (nodes of the FE mesh and control points of the VLM mesh). In order to obtain the aerodynamic loads one should know the structural response (and consequently the electrical response) which depends on the aerodynamic loads. An iterative method that accounts for the interaction between the aerodynamic and the electromechanical domains is used to solve the equations of motion. However, the aerodynamic loads and the structural motion are obtained from distinct numerical methods with distinct meshes. Therefore the structural FE nodes and the aerodynamic control points can be related as

$$\boldsymbol{\Psi}_a=\mathbf{G}\boldsymbol{\Psi} \tag{6}$$

where $\boldsymbol{\Psi}_a$ is the vector of mechanical coordinates of control points in the aerodynamic mesh, and $\mathbf{G}$ is the transformation matrix. The same transformation matrix can be used to write the structural mode shapes in terms of aerodynamic coordinates

$$\boldsymbol{\Phi}_a=\mathbf{G}\boldsymbol{\Phi} \tag{7}$$

where $\boldsymbol{\Phi}_a$ is the modal matrix in aerodynamic coordinates (corners of the vortex rings).
Since the virtual work done by the aerodynamic forces is the same for the representations in both domains, one can express

$$\delta\boldsymbol{\Psi}_a^t\mathbf{F}_a=\delta\boldsymbol{\Psi}^t\mathbf{F} \tag{8}$$

and $\mathbf{F}_a$ are the aerodynamic loads at the control points and $\mathbf{F}$ are the aerodynamic loads on the structural mesh (nodes). Using Equations (7) and (8), the equations of motion (Equations (4) and (5)) can be written as,

$$\bar{\mathbf{M}}\ddot{\boldsymbol{\eta}}+\bar{\mathbf{C}}\dot{\boldsymbol{\eta}}+\bar{\mathbf{K}}\boldsymbol{\eta}-\boldsymbol{\Phi}^t\tilde{\boldsymbol{\Theta}}v_p=\boldsymbol{\Phi}_a^t\mathbf{F}_a \tag{9}$$

$$C_p\dot{v}_p+\frac{v_p}{R_l}+\tilde{\boldsymbol{\Theta}}^t\boldsymbol{\Phi}^t\dot{\boldsymbol{\eta}}=0 \tag{10}$$

where the aerodynamic loads are transformed to the nodes of the structural mesh. In addition, the structural displacements obtained at the nodes of the FE mesh at each time step have to be obtained at the corners of vortex rings (aerodynamic mesh) for calculation of the aerodynamic loads. Hence, another transformation matrix is introduced to convert the modal coordinates to the corners of the vortex rings

$$\mathbf{x}_a=\boldsymbol{\Phi}_a^*\boldsymbol{\eta} \tag{11}$$

where $\mathbf{x}_a$ is the vector of aerodynamic coordinates and the matrices $\mathbf{\Phi}_a$ and $\mathbf{\Phi}_a^*$ are interpolated in this work using surface splines [19].

The equations of motion can be written as a system of $2n + 1$ first order ordinary-differential equations, where n is the number of vibration modes taken into account in the solution. The vector of state variables can be given as,

$$\mathbf{y} = \begin{bmatrix} \mathbf{y}_1 & \mathbf{y}_2 & y_3 \end{bmatrix}^t \tag{12}$$

where $\mathbf{y}_1 = \boldsymbol{\eta}$, $\mathbf{y}_2 = \dot{\boldsymbol{\eta}}$ and $y_3 = v_p$. Taking the derivative of $\mathbf{y}$ and using the mechanical and the electrical equations of motion (Equations (9) and (10)) one has $2n+1$ first-order ordinary-differential equations,

$$\dot{\mathbf{y}}_1 = \mathbf{y}_2 \tag{13}$$

$$\dot{\mathbf{y}}_2 = \mathbf{\Phi}_a^t \mathbf{F}_a - \bar{\mathbf{C}}\mathbf{y}_2 - \bar{\mathbf{K}}\mathbf{y}_1 - \mathbf{\Phi}^t \tilde{\mathbf{\Theta}} \mathbf{y}_3 \tag{14}$$

$$\dot{y}_3 = \frac{1}{C_p}\left(-\tilde{\mathbf{\Theta}}^t \mathbf{\Phi}^t \mathbf{y}_2 - \frac{y_3}{R_l} \right) \tag{15}$$

The $2n+1$ ordinary-differential equations with the aerodynamic loads applied at the FE nodes are then solved using a predictor-corrector scheme that accounts for the interaction between aerodynamic and electromechanical domains [17,18]. The Adams-Bashforth-Moulton predictor-corrector method is used here and a detailed description of this method can be found in the literature [20]. The predictor uses the Adams-Bashforth method and the Adams-Moulton corrector. The local truncation error is given by Milne's estimate [20] and a correction term can be included, which improves the accuracy of the result at each step.

3 Results

3.1 Structure modeled

In the case studies a cantilevered plate-like wing with two identical layers of PZT-5A is investigated. A load resistance is considered in the electric domain. The piezoaeroelastic response of the generator wing is presented here as time histories of the electrical power output and wing tip displacement for several airflow speeds and load resistances.

The input assumed in the simulations is a discrete gust disturbance. The initial conditions are set to zero and the air density is assumed to be 1.225 kg/m3.

Two identical layers of PZT-5A are embedded into the top and the bottom of the plate at the root. Conductive electrodes covering the upper and the lower faces of the piezoceramic layers are connected in series to a resistive electrical load as depicted in Fig. 1. The dimensions of the plate-like wing considered in this work are 1200 × 240 × 3 mm^3. The identical piezoceramic layers have the same width as the wing chord. The embedded piezoceramics layers cover 30% of the wing span (from the root to the tip) and each one has a thickness of 0.5 mm. The geometric and the material properties of the wing (aircraft aluminum alloy Al 2024-T3) are presented in Table 1.

Table 1. Geometric and material properties of the aluminum wing with embedded piezoceramics

Length of the wing (mm)	1200
Width of the wing (mm)	240
Thickness of the wing (mm)	3
Young's modulus of the wing (GPa)	70.0
Mass density (substructure) (kg/m^3)	2750
Proportional constant – α (rad/s)	0.1635
Proportional constant – β (s/rad)	4.17 x 10^{-4}

The typical properties of PZT-5A piezoceramics are given in Table 2.

Table 2. Material and electromechanical properties of PZT-5A

Mass density (kg/m^3)	7800
Permittivity ε_{33}^T (nF/m)	$1800\times\varepsilon_0$
c_{11}^E, c_{22}^E (GPa)	120.3
c_{12}^E (GPa)	75.2
c_{13}^E, c_{23}^E (GPa)	75.1
c_{33}^E (GPa)	110.9
c_{66}^E (GPa)	22.7
e_{31}, e_{32} (C/m^2)	-5.2
e_{33} (C/m^2)	15.9

3.2 Discrete gusts

Movements of air in turbulence are generally known as gusts [24]. Considerable evidences show that most severe gusts occur more or less as individual gusts.

In the FAR (Federal Aviation Regulation) Part 25 Section 341 are described the standards for evaluating the effects of gusts and turbulence loads on an aircraft structure.

In this paper a discrete gust is modeled using the one minus cosine approximation [21-24]. In such a case the gust field is reduced to the form of one dominant discrete gust. The shape of the gust is,

$$U = \frac{U_{ds}}{2}\left[1-\cos\left(\frac{\pi s}{H}\right)\right] \tag{16}$$

$$U_{ds} = U_{ref} F_g \left(\frac{H}{350}\right)^{\frac{1}{6}} \tag{17}$$

Where s is the distance penetrated into the gust (feet), U_{ds} is the design gust velocity and H is the gust gradient which is the distance (feet) parallel to the airplane's flight path. U_{ref} is the reference gust velocity (56 ft/s at sea level) and F_g is used to account for the fact that different aircraft configurations will react differently to the same gust. The expressions are valid for $0 \le s \le 2H$.

According to static Pratt-Walker formula value of H should be 12.5 chords, considering the wing used for simulation (chord length of 0.24 meters). However, the value of H equal to 5 feet and U_{ds} of 3.0 feet is used in this work.

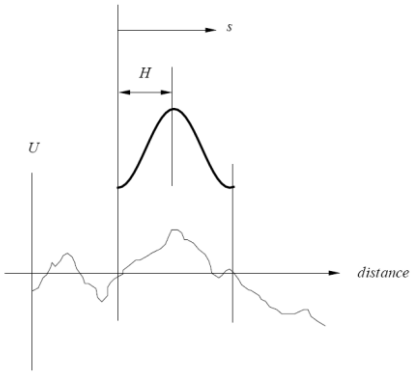

Fig. 3. – A discrete (1-cos) gust shape within a larger continuous turbulence profile

3.3 Results

Among the solutions obtained, we present results for the short circuit flutter speed of the continuous electrodes configuration and short circuit flutter speed of the segmented electrodes configuration. Continuous electrodes covering the piezoceramic layers (poled in the opposite directions) are connected in series to a resistive electrical load (Figure 1) in the first case. Later, the electrodes are segmented on the center line (mid-chord position) and properly combined to the resistive electrical load to avoid the cancelation of electrical output of the bending and the torsion modes. The piezoaeroelastic response characteristics of the continuous and the segmented electrode cases are for five different values of load resistance in the electrical domain.

The time history of power output at the short-circuit flutter speed (40 m/s) for the continuous-electrode case is shown in Figure 4. The power output increases as the value of load resistance

is increased from short-circuit condition to $R=10^4\Omega$. Clearly the value of the load resistance $R=10^4\Omega$ provides the maximum power output among the set of load resistance values considered here. Note that the largest power output case also exhibits a decaying behavior which is due to the shunt damping effect of power generation. If the load resistance is increased the power output decreases. At the open-circuit condition the power output is similar to the ones obtained close to short-circuit.

The time history of power output for the segmented electrode condition at the short-circuit flutter speed of the continuous electrode configuration is shown in Figure 5a. The peak power obtained is larger than the peak power obtained from the continuous electrodes solution (with the set of load resistances considered here). Cancelation of the electrical output from torsion modes is avoided with segmented electrodes.

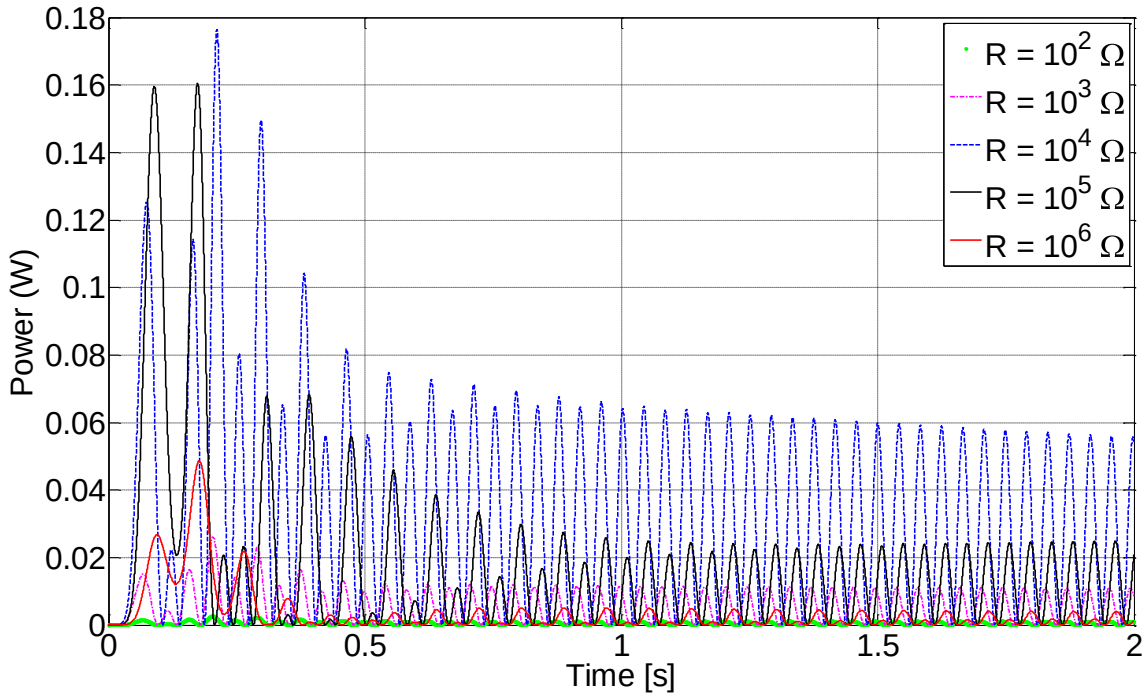

Fig. 4. Power output for five different values of load resistance using continuous electrodes at 40 m/s (flutter) speed.

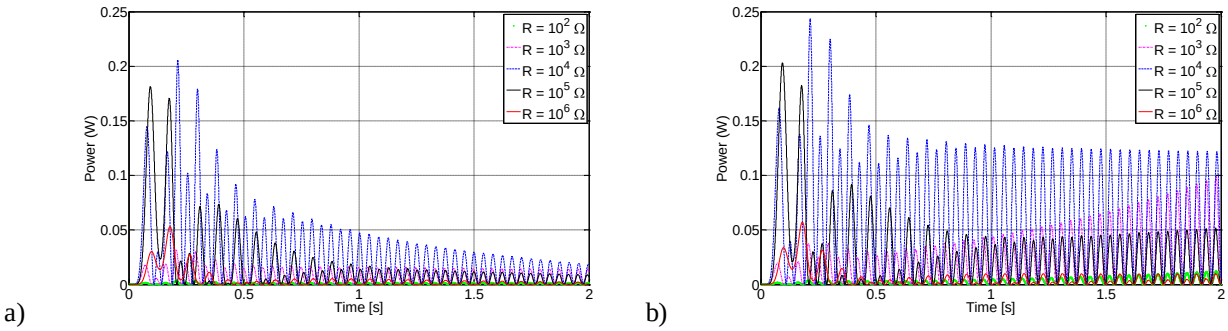

Fig. 5. Power output for five different values of load resistance using segmented electrodes at a) 40 m/s speed, b) flutter speed (41 m/s)

The time history of power output for the segmented electrodes case at 41 m/s and is shown in Figure 5b. The power output is continuously extracted over the time and the peak power observed in Figure 5a is larger than that of the previous cases (continuous and segmented electrodes at 40 m/s). The optimum load resistance ($R = 10^4 \Omega$) gives the maximum power with the segmented electrodes.

The power histories for the optimum load resistance of the continuous and segmented electrodes cases are presented in Figure 6 at the flutter speed (40 m/s for continuous electrode and 41 m/s for segmented electrodes). One can observe that flutter speed is increased with the segmented electrodes configuration as well as peak power is almost twice the continuous electrode configuration.

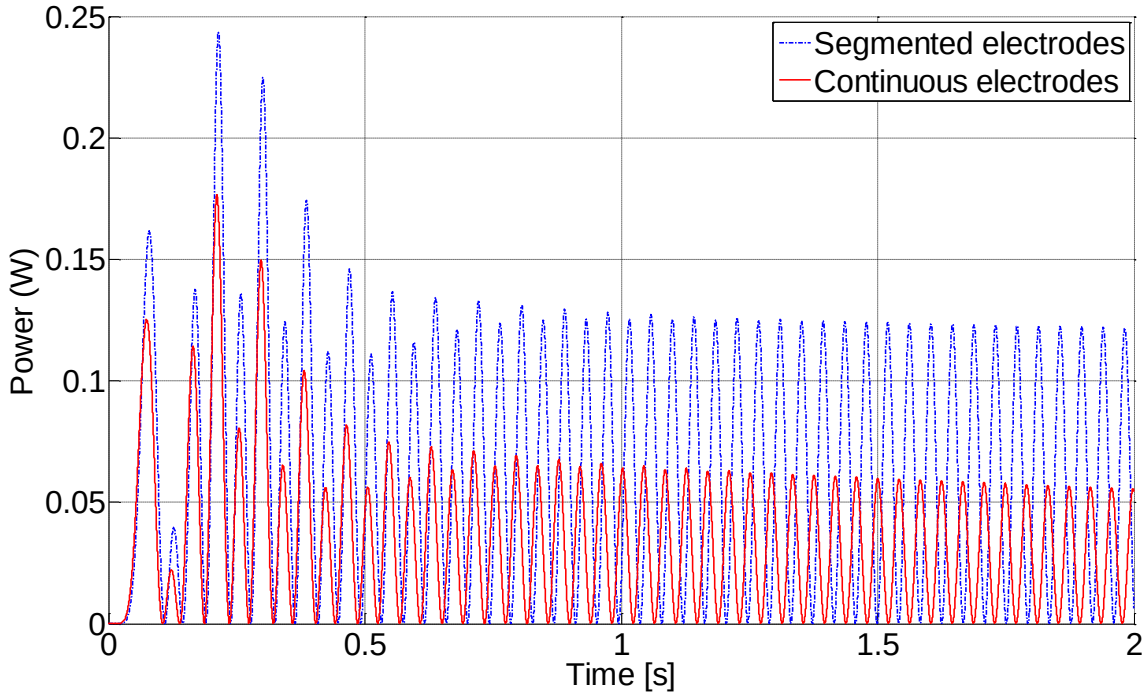

Fig. 6. Comparative values of Power output using continuous and segmented electrodes at flutter speed

4 Conclusions

In this paper the piezoaeroelastic modeling of a generator wing with continuous and segmented electrodes is presented. The response of the wing to a discrete gust (1-cos) disturbance is investigated. A slight increase in flutter speed (1 m/s) and larger power output is observed when using the segmented electrodes configuration. In such case the electromechanical coupling is improved and the cancellation of the electrical output of torsion motions is avoided. The optimum load resistance of (among the ones studied here) gives the maximum power and shunt damping effect for continuous and segmented electrodes cases. This piezoaeroelastic model was used in a previous work and a sharp-edge gust was used. The response to a discrete gust results in better power then the sharp edge gust previously investigated.

5 Acknowledgements

The authors gratefully acknowledge CNPq and FAPEMIG for funding the present research work through the INCT-EIE.

References

[1] Langelaan, J.W., 2007, "*Long Distance/Duration Trajectory Optimization for Small UAVs*", AIAA Guidance, Navigation and Control Conference and Exhibit.

[2] Anton, S.R. and Inman D.J., "*Vibration energy harvesting for unmanned air vehicles*", Proceedings of SPIE 6928, March 10-13, San Diego, CA (2008).

[3] Magoteaux, K.C., Sanders, B. and Sodano, H.A., "*Investigation of energy harvesting small unmanned air vehicle*", Proceedings of SPIE 6928, March 10-13, San Diego, CA (2008).

[4] De Marqui, Jr., C., Erturk, A., and Inman, D.J. 2010 "*Piezoaeroelastic Modeling and Analysis of a Generator Wing with Continuous and Segmented Electrodes*", Journal of Intelligent Material Systems and Structures, in publication.

[5] De Marqui, Jr., C., Vieira, W.G.R, Erturk, A., and Inman, D.J. 2010 "*Modeling and Analysis of Piezoelectric Energy Harvesting from Aeroelastic Vibrations Using the Doublet-Lattice Method*", Journal of Vibration and Acoustics, in publication.

[6] Erturk, A., Renno, J.M. and Inman, D.J., "*Modeling of piezoelectric energy harvesting from an L-shaped beammass structure with an application to UAVs*", Journal of Intelligent Material Systems and Structures 20, 529-544 (2009).

[7] Junhui Hu, Januar Jong, and Chunsheng Zhao, "*Vibration Energy Harvesting Based on Integrated Piezoelectric Components Operating in Different Modes"*, IEEE Transactions on Ultrasonics, Ferroelectrics, and Frequency Control, vol. 57, no. 2, February 2010

[8] Erturk, A. (2009), "*Electromechanical Modeling of Piezoelectric Energy Harvesters"*, Dissertation, Virginia Polytechnic Institute and State University, Blacksburg, VA

[9] De Marqui, Jr., C., Erturk, A., and Inman, D.J., "*An electromechanical finite element model for piezoelectric energy harvester plates"*, Journal of Sound and Vibration 327 pp 9-25

[10] Arnau, A., "*Piezoeletric Transducers and Applications"* (2008)

[11] Heywang,W., Lubitz, K., Wersing, W., "*Piezoelectricity: Evolution and Future of a Technology"* (2008)

[12] Umeda, M., Nakamura, K. and Ueha, S., 1996. "*Analysis of Transformation of Mechanical Impact Energy to Electrical Energy using a Piezoelectric Vibrator"*, Japanese Journal of Applied Physics, Part 1, 35(5B):3267–3273.

[13] Xu, C.N., Akiyama, M., Nonaka, K. and Watanabe, T. 1998. "*Electrical Power Generation Characteristics of PZT Piezoelectric Ceramics"*, IEEE Transaction on Ultrasonics, Ferroelectrics and Frequency Control, 45(4):1065–1070.

[14] Goldfarb, M. and Jones, L. D. 1999. "*On the Efficiency of Electric Power Generation with Piezoelectric Ceramic"*, ASME Journal of Dynamic Systems, Measurement, and Control, 121:566–571.

[15] Erturk, A., and Inman, D.J., "*A Distributed Parameter Electromechanical Model for Cantilevered Piezoelectric Energy Harvesters"*, Journal of Vibration and Acoustics (August 2008), Vol. 130 / 041002-1

[16] Erturk, A., and Inman, D.J., "*Issues in mathematical modeling of piezoelectric energy harvesters"*, Smart Mater. Struct. 17 (2008) 065016 (14pp)

[17] Katz J and Plotkin A 2001, "*Low Speed Aerodynamics"* (Cambridge University Press)

[18] Benini G R, Belo E M and Marques F D 2004 "*Numerical Model for the Simulation of Fixed Wings Aeroelastic Response"*, Journal of the Brazilian Society of Mechanical Sciences & Engineering 26 129-136

[19] Harder R L, Desmarais R N 1972, "*Interpolation using surface splines"*, Journal of Aircraft 9 pp. 189-191

[20] Lambert J D 1991, "*Numerical Methods for Ordinary Differential Systems: The Initial Value Problem"* (Chichester: Wiley)

[21] Chudý, P., "*Response of a Light Aircraft Under Gust Loads"*, Acta Polytechnica, Vol. 44 No. 2/2004

[22] *"An introduction to rigid aeroplane response to gusts and atmospheric turbulence"*, IHS/ESDU 04024 (Nov. 2004)

[23] Federal Aviation Administration - *Code of Federal Regulations - Part. 25 / Sec. 25.341* / http://rgl.faa.gov/Regulatory_and_Guidance_Library/rgFAR.nsf/0/156ccf55583a0ac985256672004ec0d4!OpenDocument / (Acessed April 2010)

[24] Wah NG, T., *MAE3407 Aircraft Structures II / Chapter 4 - Basic Airframe Loads* http://biofuturex.com/mae3407/ (Acessed April 2010)

Copyright Statement